PHYSICAL REVIEW D **80,** 124007 (2009)

Bowen-York trumpet data and black-hole simulations

Mark Hannam,[1] Sascha Husa,[2] and Niall Ó Murchadha[1]

[1]*Physics Department, University College Cork, Cork, Ireland*

[2]*Departament de Física, Universitat de les Illes Balears, Cra. Valldemossa Km. 7.5, Palma de Mallorca, E-07122 Spain*

(Received 21 August 2009; published 4 December 2009)

The most popular method to construct initial data for black-hole-binary simulations is the puncture method, in which compactified wormholes are given linear and angular momentum via the Bowen-York extrinsic curvature. When these data are evolved, they quickly approach a trumpet topology, suggesting that it would be preferable to use data that are in trumpet form from the outset. To achieve this, we extend the puncture method to allow the construction of Bowen-York trumpets, including an outline of an existence and uniqueness proof of the solutions. We construct boosted, spinning and binary Bowen-York puncture trumpets using a single-domain pseudospectral elliptic solver, and evolve the binary data and compare with standard wormhole-data results. We also show that for boosted trumpets the black-hole mass can be prescribed *a priori*, without recourse to the iterative procedure that is necessary for wormhole data.

DOI: 10.1103/PhysRevD.80.124007 PACS numbers: 04.20.Ex, 04.30.Db, 95.30.Sf

I. INTRODUCTION

Numerical solutions of the full Einstein equations for the last orbits and merger of compact binary systems are important for the developing field of gravitational-wave astronomy. In the case of black-hole binaries, long-term simulations became possible in 2005 [1–3], and within the last few years the field has developed to the point where the gravitational-wave (GW) signal from such systems can be calculated to essentially the required accuracy of current GW detectors [4], and work is underway to incorporate these results into GW searches [5]. However, only a small fraction of the full black-hole-binary parameter space has yet been studied [6], and its full exploration will require yet more accurate and efficient numerical simulations. The first step in any simulation is the production of initial data, and these determine in part the accuracy and physical fidelity of the final simulation; that is the focus of this paper.

The $3+1$ approach to solving Einstein's equations consists of specifying initial data (the metric and its time derivative on one constant-time slice of spacetime), and then evolving that data forward in time. Valid initial data satisfy a set of constraint equations, and a given solution to the constraints will represent a certain physical situation in a certain set of coordinates. We are then faced with the problem of finding constraint-satisfying data that both represent the physical situation we wish to simulate (in our case two black holes following noneccentric inspiral) *and* are in a suitable set of coordinates.

The most widely used method to evolve black-hole-binary initial data is the moving-puncture method [2,3], which involves a modification of the Baumgarte-Shapiro-Shibata-Nakamura (BSSN) [7,8] formulation of the $3+1$ ADM-York Einstein equations [9,10] combined with the "$1+\log$" [11] and "$\tilde{\Gamma}$-driver" gauge conditions [12,13].

As the name suggests, the data that are usually evolved with this method are puncture data [14], whereby black holes are represented on the numerical grid by compactified wormholes. However, when these data are evolved using the standard moving-puncture method the numerical slices lose contact with the extra asymptotically flat wormhole ends, and quickly asymptote to cylinders of finite areal radius located within the horizon of each black hole. That the data evolve to these "trumpets" was realized in [15], in which an analytic stationary trumpet end state was derived and shown to agree with numerical results.

That work suggested a new form of initial data, based on trumpets. It was shown in [16] that maximally-sliced trumpet data can easily be constructed numerically based on the solution first presented in [17], and that these data are indeed time independent in a moving-puncture simulation. These data represent the first nontrivial test solution for most current black-hole evolution codes. It was later shown in [18] that an implicit form of the same solution could be constructed analytically, and in [19] the corresponding solution for the $1+\log$-sliced case was found.

We have presented a detailed study of Schwarzschild wormholes and trumpets in [19], with a focus on constructing and evolving Schwarzschild trumpet-puncture data. This work extends that study to boosted, spinning and binary trumpets. As we described in the concluding section of [19], ideal binary puncture data will be in trumpet form, $1+\log$-sliced (or satisfy whatever slicing condition is ultimately used to evolve them), and represent true boosted Schwarzschild or Kerr black holes (i.e., will be free of the junk radiation that plagues all current binary simulations). As a first step in a larger research program to attempt to achieve that goal, we deal here with only the first point in our list of requirements: that the data be in trumpet form. The data we construct will not meet *any* of the other

requirements: they will be maximally (not 1 + log) sliced, and they will be conformally flat, meaning that they include essentially the same junk radiation as standard puncture data. As such, this work is a proof-of-principle exercise that demonstrates that is feasible to produce binary trumpet data. Along the way a number of new issues arise that are not present in the wormhole case, and variants of these issues may recur in efforts to produce yet more general data.

We will start with a brief summary of wormholes, trumpets and punctures in Sec. II, then discuss in some detail the maximal slicing case in spherical symmetry in Sec. III as an example for our analytical setup to construct trumpet data and for our numerical algorithm. We then extend the trumpet-puncture construction to boosted (Sec. IV) and spinning (Sec. V) Bowen-York black holes, and provide an outline of a proof for both existence and uniqueness of these solutions. In Sec. VI we estimate the junk-radiation content of these initial-data sets, before moving on to binary data in Sec. VII. The ultimate goal is of course to produce data that can be used in black-hole-binary simulations, and in Sec. VIII we evolve a binary data set and compare with the corresponding standard wormhole-puncture results. We close with a discussion on the next steps to producing optimal initial data for moving-puncture simulations.

II. BACKGROUND: A BRIEF SUMMARY OF WORMHOLES, TRUMPETS AND PUNCTURES

A. Wormhole-puncture data

Consider a constant-time slice of the Schwarzschild spacetime. Write the standard Schwarzschild solution in isotropic coordinates, i.e.,

$$ds^2 = -\left(\frac{1-\frac{M}{2r}}{1+\frac{M}{2r}}\right)^2 dt^2 + \psi^4(dr^2 + r^2 d\Omega^2), \qquad (1)$$

and the isotropic coordinate r is related to the Schwarzschild areal radial coordinate R by

$$R = \psi^2 r, \qquad (2)$$

and $\psi = 1 + M/2r$ is a conformal factor. Now the data (γ_{ij}, K_{ij}) on any $t =$ constant slice are given by $\gamma_{ij} = \psi^4 \eta_{ij}$ (where η_{ij} is the flat-space metric in the chosen coordinate system) and $K_{ij} = 0$. The fact that the physical spatial metric can be related to the flat-space metric using only the conformal factor indicates that the solution is *conformally flat*.

We see immediately from Eq. (2) that the slice does not reach the physical singularity at $R = 0$, or even penetrate the black-hole horizon at $R = 2M$. In fact, the coordinate range $r \in [0, \infty]$ contains two copies of the Schwarzschild spacetime exterior to $R = 2M$: one copy in $r \in [0, M/2]$ and the other in $r \in [M/2, \infty]$. These coordinates therefore represent the exterior Schwarzschild spacetime as a wormhole, and this is most clear when viewed in an embedding diagram like that shown in Fig. 1 of [19].

The advantage of these slices for numerical relativity is that the entire exterior space can be represented on R^3 without any need to deal explicitly with the physical singularity of the black hole, or to "excise" any region of the computational grid. The point $r = 0$, which is commonly referred to as a "puncture" [14], represents a second copy of spatial infinity, but the solution is well-behaved there, except for the conformal-factor ψ, which diverges as $1/r$.

We can write initial data for multiple Schwarzschild black holes simply by modifying the conformal factor to $\psi = 1 + \sum_i m_i/(2r_i)$, where the m_i parametrize the mass of the ith black hole, and the ith puncture is located at $r_i = 0$ [20]. Furthermore, one may imbue these black holes with linear and angular momentum by providing a nonzero extrinsic curvature. If we retain the property of conformal flatness and choose the extrinsic curvature to be tracefree ($K = 0$, or *maximal slicing*), then there exist solutions of the momentum constraint for boosted and/or spinning black holes; these are the Bowen-York solutions [21]. The solution is provided only in the conformal space, and is related to the physical extrinsic curvature by

$$K_{ij} = \psi^{-2} \tilde{A}_{ij}, \qquad (3)$$

where here $\tilde{A}_{ij}$ is the Bowen-York solution. Now, however, the conformal factor is not known analytically, and can only be found by solving numerically the Hamiltonian constraint,

$$\tilde{\nabla}^2 \psi + \frac{1}{8} \psi^{-7} \tilde{A}_{ij} \tilde{A}^{ij} = 0. \qquad (4)$$

The most convenient way to solve (4) is by the "puncture method" [14], which is to realize that the solution can be constructed conveniently in terms of a (typically small) correction u to the Brill-Lindquist solution,

$$\psi = 1 + \sum_i \frac{m_i}{2r_i} + u. \qquad (5)$$

Since the Brill-Lindquist conformal factor is in the kernel of the flat-space Laplacian, the Hamiltonian constraint is now an equation for the correction function u:

$$\tilde{\nabla}^2 u + \frac{1}{8} \psi^{-7} \tilde{A}_{ij} \tilde{A}^{ij} = 0. \qquad (6)$$

Furthermore, the function u is sufficiently regular over all of R^3 that (6) is in the form of a nonlinear elliptic equation that is straightforward to solve by a number of standard methods. This approach is used to construct the majority of black-hole-binary initial data used in current numerical simulations, and the elliptic solve is performed either with mesh-refinement finite-difference solvers [22] or, in most cases, by an elegant single-domain spectral approach [23], which we will adopt for the work presented here.

A key property of the Bowen-York family of solutions to the momentum constraint is that the values of the momentum and angular momentum of the spacetime (and thus in some sense the momenta and spins of the black holes) can be prescribed *before* solving for the conformal factor.

Two further properties of these data deserve particular attention here, and we will return to them when comparing these wormhole-puncture data with our new trumpet-puncture data in the following sections.

First, Bowen-York black holes are conformally flat, which is not the case for either a true boosted Schwarzschild black hole, or a Kerr black hole, or a boosted Kerr black hole. Since it is usually a boosted Schwarzschild or Kerr black hole that we really wish to describe, these data are often described as the desired physical objects plus some "junk"; the junk represents a valid part of a solution of Einstein's equations, but it is not a part that we would expect to occur physically, and can be interpreted as unphysical gravitational-wave content. As the data evolve forward in time, the junk either falls into the black hole or radiates away, quickly leaving precisely the physical situation that was intended in the first place, albeit with slightly different physical parameters.

In practice (i.e., in black-hole-binary simulations) this junk radiation causes two problems. One is that it introduces noise into the numerical simulation, which can affect the numerical accuracy. This point is clearly illustrated in [24]. The other is that it limits the physical black-hole spin that can be achieved. When the spin angular momentum of the Bowen-York black hole is extremely high, most of the angular momentum manifests itself as junk, and after that junk has either fallen into the black hole or radiated away, we are left with a Kerr black hole that has spin no higher than $a/M = S/M^2 \leq 0.93$ [25–27]; we will confirm this with high-precision numerical simulations, bounding the final Kerr parameter at $a/m \leq 0.929$. This property of Bowen-York data preclude their use to study very highly spinning black holes, which may in fact be the most common astrophysically [28–30], and we must turn to other types of data—see, for example, [31] for the construction and evolution of spinning but nonboosted puncture data, and [27] for non-conformally-flat black-hole initial data where the interior of the black hole is excised.

The other property of Bowen-York puncture data that we want to highlight is the calculation of the black-hole mass. Having produced data for two black holes, we would like to know what their masses are; although the parameters m_i parametrize the black-hole masses, the black-hole mass equals the mass parameter only in the case of a single Schwarzschild black hole, i.e., the original Schwarzschild solution in isotropic coordinates.

In any other case, we typically estimate the black-hole mass by two methods. One is to calculate it from the area of the apparent horizon. This requires that we first locate the apparent horizon, which can be computationally expensive (although fast and efficient solvers exist, for example [32]). The other method is to make an inversion transformation at each puncture and calculate the ADM mass at that black hole's extra asymptotically flat end, and to treat this quantity as the black-hole mass. For a binary system, this mass estimate is given by

$$M_i = m_i\left(1 + u_{0,i} + \frac{m_i m_j}{2D_{ij}}\right), \tag{7}$$

where D_{ij} is the coordinate separation between the two punctures, and $u_{0,i}$ is the value of the correction function u at the ith puncture. Remarkably, this expression is found to agree within numerical error with the mass calculated from the apparent horizon [33,34], although we will see in Sec. VI that this can only be expected to hold for boosted black holes, or black holes with small spins.

B. Trumpet-puncture data

Bowen-York puncture data were first constructed long before stable numerical simulations of black-hole binaries were possible, and were useful in both mathematical relativity [35–37] and in studies of initial data [14,38–41]. However, with the advent of the moving-puncture method [2,3] it was found that wormholes may not be the most suitable topology for black-hole initial data.

In a moving-puncture simulation, the numerical slices quickly lose contact with the extra asymptotically flat ends, and instead asymptote to cylinders of finite areal radius [15,16,19,42–44], or trumpets. This suggests that it would be more natural to construct initial data in trumpet form from the outset.

To date this has only been done for a single Schwarzschild black hole. The question addressed in this paper is, How can we generalize the wormhole-puncture procedure to produce *trumpet* punctures for black-hole binaries? For a single maximally-sliced Schwarzschild black hole, the trumpet-data can be put in a form similar to the wormhole isotropic coordinates, where now the conformal factor behaves as $\psi \sim \sqrt{3M/2r}$ near the puncture. However, the full conformal factor is not known analytically (except as an implicit equation in terms of the Schwarzschild radial coordinate R) [15,19]. This means that it is not straightforward to superpose two trumpets as with the Brill-Lindquist solution in the wormhole case. And it is not obvious how the introduction of the Bowen-York extrinsic curvature (which, if we retain conformal flatness and maximal slicing, remains a valid solution of the momentum constraint), affects the behavior of the conformal factor near the puncture, or the physical properties of the data. Finally, without the presence of extra asymptotically flat ends, we lose the simple procedure to estimate the black hole's mass from Eq. (7). These are the issues that we address in this work.

In Sec. III we describe in more detail the maximal Schwarzschild trumpet, and use it to illustrate our more general method for producing single-trumpet data.

III. MAXIMAL SCHWARZSCHILD TRUMPET

A. Constructing a conformal-factor ansatz for trumpet data

The basis of this work are data that represent a maximal slice of the Schwarzschild spacetime with a trumpet topology. The first hints of this representation of Schwarzschild were given by Estabrook *et al.* [17] in 1973, but it wasn't until the development of the moving-puncture method [2,3] in 2005, and a subsequent understanding of the dynamical behavior of the numerical slices [15] in that method, that it was realized that the maximal Schwarzschild trumpet could be expressed in a simple form [16], and could in turn be written in the puncture isotropic coordinates suited to moving-puncture simulations [16,18].

For a single Schwarzschild black hole with mass M, the conformal initial data in Cartesian coordinates are

$$\tilde{\gamma}_{ij} = \delta_{ij}, \qquad \tilde{A}^S_{ij} = \frac{C}{r^3}(3n_i n_j - \delta_{ij}), \qquad K = 0,$$

$$\alpha = \sqrt{1 - \frac{2M}{R} + \frac{C^2}{R^4}}, \qquad \beta^i = \frac{x^i \alpha C}{R^3},$$

where $C = \sqrt{27/16}M^2$, R is the Schwarzschild radial coordinate, $r = (x^2 + y^2 + z^2)^{1/2}$ is the isotropic radial coordinate, and $n_i = x_i/r$ is the outward-pointing normal vector. All that remains to fully specify the initial data is a valid conformal-factor ψ that maps these data to the physical space, i.e.,

$$\gamma_{ij} = \psi^4 \tilde{\gamma}_{ij} \qquad K_{ij} = \psi^{-2}\tilde{A}^S_{ij} + \frac{1}{3}\psi^4 \tilde{\gamma}_{ij} K$$

$$R = \psi^2 r.$$

The conformal factor must satisfy the Hamiltonian constraint and asymptote to $\psi \to 1$ as $r \to \infty$. A numerical solution of the Hamiltonian constraint for these data was first presented in [16], and an analytic solution (albeit an implicit solution in terms of R, not r) given in [18].

To illustrate the method that we will use for more general cases, and to test our elliptic solver, we will again solve the Hamiltonian constraint numerically. Our boundary conditions are that $\psi \to 1$ as $r \to \infty$, and $\psi \sim \sqrt{3M/2r}$ as $r \to 0$; the latter condition ensures that we have a trumpet topology.

In order to solve the Hamiltonian constraint, we start with an ansatz for ψ that includes the required asymptotic behavior. We write the full conformal factor that solves the Hamiltonian constraint as

$$\psi = \psi_s + u, \tag{8}$$

where ψ_s incorporates the desired asymptotics. The Hamiltonian constraint for this problem is

$$\tilde{\nabla}^2 u = -\frac{1}{8}\psi^{-7}\tilde{A}_{ij}\tilde{A}^{ij} - \tilde{\nabla}^2 \psi_s, \tag{9}$$

where $\tilde{\nabla}^2$ represents the Laplacian with respect to the flat background metric, and it is understood that $\tilde{A}_{ij} = \tilde{A}^S_{ij}$, although this is the form of the Hamiltonian constraint that we will deal with for all choices of $\tilde{A}_{ij}$ throughout this paper.

One easy way to incorporate the asymptotic behavior is to apply weight functions to the two asymptotic conditions,

$$\psi_s(r) = w_1(r)\sqrt{\frac{3M}{2r}} + w_2(r)$$

such that

$$w_1(0) = 1, \qquad w_1(\infty) = 0,$$
$$w_2(0) = 0, \qquad w_2(\infty) = 1.$$

The weight functions we choose are

$$w_1(r) = \frac{1}{1 + r^4}, \qquad w_2(r) = \frac{r^4}{1 + r^4}.$$

These have the property that at each end of the slice the conformal factor's lowest-order deviation from the required behavior is at fourth order.

Consider now the behavior of the conformal factor near the puncture. We assume the leading order terms to be of the form

$$\psi = \frac{A}{r^{1/2}} + Br^n. \tag{10}$$

If we insert this ansatz into the Hamiltonian constraint, we have

$$\tilde{\nabla}^2\psi = -\psi^{-7}\frac{81M^4}{64r^6} \Rightarrow$$
$$-\frac{A}{4r^{5/2}} + Bn(n+1)r^{n-2} = \frac{81M^4}{64A^7 r^{5/2}} \times \left(1 - \frac{7B}{A}r^{n+1/2} + \ldots\right),$$

where we have expanded about $r = 0$ on the right-hand side. Equating coefficients of r, we find that $A = \sqrt{3M/2}$ (as we expect). We also find that for a consistent solution $n = \sqrt{2} - 1/2 = 0.9142\ldots$ and B remains undetermined. We therefore see that divergent terms near the puncture do exactly cancel, and the next-to-leading order term goes to zero. However, this next-to-leading order term goes to zero with a nonrational power of r (which was also noted in [45]), and this may limit the accuracy of a spectral solution to (9). If this is the case, we may also include the $r^{\sqrt{2}-1/2}$ behavior into our ansatz.

An implicit solution of ψ in terms of the Schwarzschild radial coordinate R is given in [18], as is an implicit solution of $r(R)$. If we combine these as $(\psi(R) - \sqrt{3M/2r(R)})/r(R)^{\sqrt{2}-1/2}$, and take the limit as $R \to 3M/2$, we can determine the coefficient B in our ansatz above. We find that

$$B = \left(\frac{3M}{2}\right)^{3/2}\left(M + \frac{3M}{2\sqrt{2}}\right)^{-1-\sqrt{2}}. \tag{11}$$

If necessary, we may now use

$$\psi_s(r) = w_1(r)\left(\frac{A}{\sqrt{r}} + Br^{\sqrt{2}-1/2}\right) + w_2(r), \tag{12}$$

as the ansatz in our numerical solution of the Hamiltonian constraint.

To summarize, we have two choices of conformal-factor ansatz that we may adopt, and which we denote by,

$$\psi = \psi_{s1}(r) + u = w_1(r)\sqrt{\frac{3M}{2r}} + w_2(r) + u, \tag{13}$$

$$\psi = \psi_{s2}(r) + u = w_1(r)\left(\frac{A}{\sqrt{r}} + Br^{\sqrt{2}-1/2}\right) + w_2(r) + u. \tag{14}$$

B. Numerical solution of the Hamiltonian constraint

In order to solve the equations numerically, we have written a code to solve systems of nonlinear elliptic equations with general finite-difference methods in three spatial dimensions. In this work we will only utilize this solver with pseudospectral discretizations, representing the solution by Fourier series in (periodic) angular coordinates, and as Chebyshev polynomials otherwise. The solver has been developed as a Mathematica package, it uses the Mathematica `LinearSolve` function with a Krylov method and ILU preconditioner to solve Linear systems, and Newton iteration to deal with nonlinearities. This approach has allowed us to develop a very flexible spectral elliptic solver from scratch, in order to achieve good performance even for the larger grids we use in this paper. We consistently use sparse matrix objects and generate compiled code using Mathematica's `CompiledFunction` for certain key functions which operate on individual matrix elements.

The elliptic solver uses compactified coordinates (X, Y, ϕ), with $X \in [-1, 1]$, $Y \in (-1, 1)$ and $\phi \in (-\pi, \pi)$. In all cases that involve a single black hole, we transform to these coordinates from spherical polar coordinates with $r = (1 - X)/(1 + X)$ and $Y = \cos(\theta)$, so that $X = -1$ corresponds to $r \to \infty$ and $X = 1$ corresponds to $r = 0$. In order for the coefficients of the Laplacian operator to be sufficiently smooth over the entire domain, the entire equation is weighted by a factor

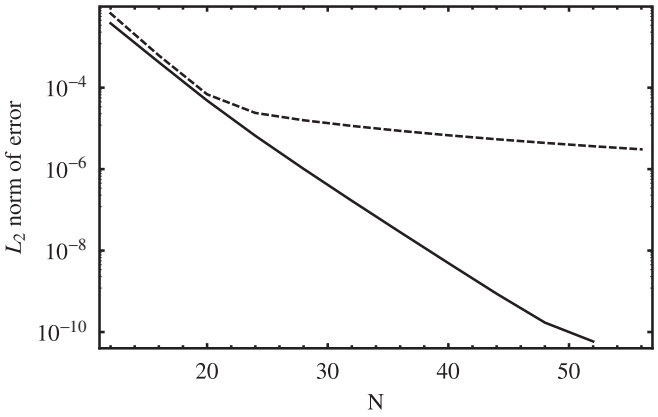

FIG. 1. The L_2 norm of the error in the solution function u for a maximal Schwarzschild trumpet. The dashed line shows the error when using the ansatz (13), while the solid line shows the error when using the ansatz (14), which includes the next-to-leading order behavior in the conformal factor near the puncture.

$$w_3(X, Y, \phi) = \frac{(1 + X)^3(1 - Y^2)}{(1 - X)^2}. \tag{15}$$

The accuracy of the numerical method is demonstrated in Fig. 1, which shows the L_2 norm of the error between the numerical and analytic solutions as a function of the number of collocation points N. (The same number of points is chosen in each direction, although since this solution is spherically symmetric, the solution varies only along the X direction.) It is clear from Fig. 1 that the spectral convergence is lost for $N > 20$ when the ansatz ψ_{s1} is used, but remains up to at least $N = 48$ where the next-to-leading order behavior is included in ψ_{s2}.

The numerical solution u is shown in Fig. 2. Solutions using both the ψ_{s1} and ψ_{s2} Ansätze are shown. The second panel in the figure zooms into the region near the puncture. In this figure the solution was produced using the ansatz with ψ_{s2}. We can see that the function smoothly approaches zero at the puncture, and is well resolved by the numerical method. The ψ_{s2}-based solution is not well resolved near the puncture and is not included in the second panel. The data in this plot are from solutions with $N = 52$ collocation points.

IV. SINGLE BOOSTED BOWEN-YORK TRUMPET

We now consider a single trumpet with linear momentum.

To do this we add to the conformal extrinsic curvature the Bowen-York solution for a single black hole with linear momentum P^i,

$$\tilde{A}^{\mathrm{BY}}_{ij}(r; \mathbf{P}) = \frac{3}{2r^2}(P_i n_j + P_j n_i - (\delta_{ij} - n_i n_j)P^k n_k), \tag{16}$$

so that the total conformal extrinsic curvature is

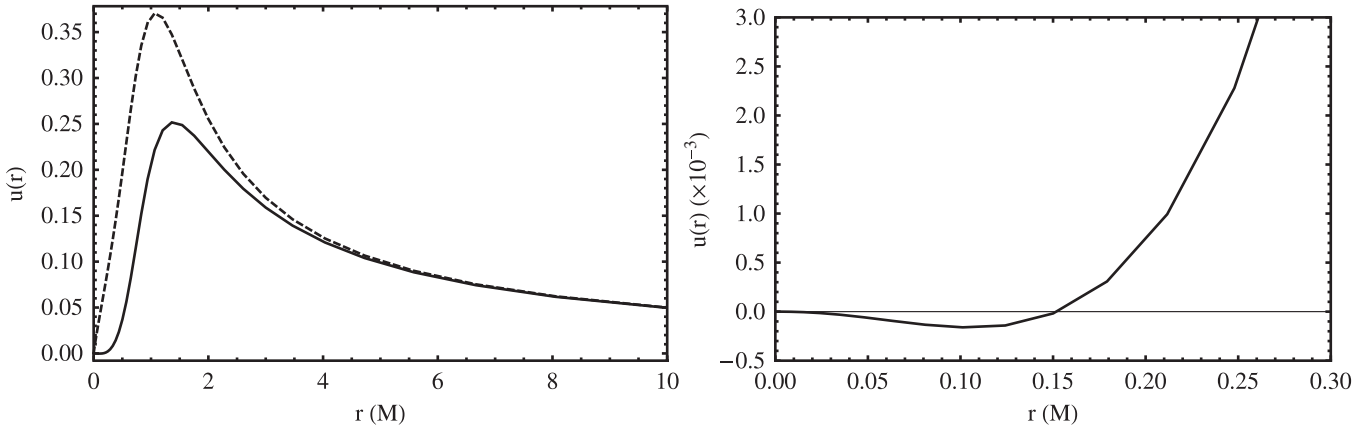

FIG. 2. The correction function u for the maximal Schwarzschild trumpet, for the solution with $N = 52$ collocation points. The solution using the ψ_{s1} ansatz (13) is shown with a dashed line, and the solution using the ψ_{s2} ansatz (14) is shown with a solid line. The second panel zooms into the region near the puncture, to illustrate that the ψ_{s2}-based solution smoothly approaches zero there, and is well resolved; the ψ_{s1} solution is poorly resolved in this region.

$$\tilde{A}_{ij}^{\mathrm{BYT}}(r;\mathbf{P}) = \tilde{A}_{ij}^{S}(r;\mathbf{P}) + \tilde{A}_{ij}^{BY}(r;\mathbf{P}). \tag{17}$$

The superscript "BYT" is a reminder that this is a Bowen-York trumpet.

Note the asymptotic behavior of $\tilde{A}_{ij}^{\mathrm{BY}}$ as $r \to 0$: it diverges as $1/r^2$. Since the trumpet extrinsic curvature diverges faster, as $1/r^3$, it dominates the Hamiltonian constraint near the puncture, and so determines the behavior of the solution. In particular, this means that the trumpet form $\psi \sim \sqrt{3M/2r}$ remains.

Consider the general form of $\tilde{A}_{ij}\tilde{A}^{ij}$ for the boosted case (in the following we will suppress the angular dependence of the functions for simplicity): the contribution from the Schwarzschild trumpet diverges as r^{-6}, the Bowen-York contribution diverges as r^{-4}, and the cross terms diverge as r^{-5}, so we have

$$\tilde{A}_{ij}\tilde{A}^{ij} = \frac{A_4}{r^4} + \frac{A_5}{r^5} + \frac{A_6}{r^6}. \tag{18}$$

where A is the same quantity that was introduced in Eq. (10).

Near the puncture, we can write the inverse conformal-factor term as

$$\begin{aligned}\psi^{-7} &= (Ar^{-1/2} + u)^{-7} = A^{-7}r^{7/2}(1 + ur^{1/2}/A)^{-7} \\ &= A^{-7}r^{7/2} - 7A^{-8}ur^4 + O(r^{9/2}),\end{aligned}$$

where A is the same quantity that was introduced in Eq. (10). We can now write out the source term of the Hamiltonian constraint as

$$\frac{1}{8}\psi^{-7}\tilde{A}_{ij}\tilde{A}^{ij} = \sum_{i=0}^{2}\frac{D_i}{r^{1/2+i}} + \sum_{i=0}^{2}\frac{uD_i'}{r^i}. \tag{19}$$

The D_2 term is the one that diverges as $r^{-5/2}$ and is canceled by a corresponding term from the Laplacian of ψ_s, as described in Sec. III. The remaining terms all result in contributions to u with positive powers of r, and which therefore go to zero at the puncture, *except* for the D_2' term, which can in principle lead to a contribution that diverges as $\ln r$. We note that such a term also appears in the Schwarzschild case (with our choice of ansatz), but there we know that $u = 0$ at the puncture, and so none of the D_i' terms contribute to the solution. Fortunately, we will see in the existence proof that we present below that the same is true in the boosted case. In the coordinates of our elliptic solver, the puncture $r = 0$ is located on the entire coordinate plane $X = -1$, and so there we can simply impose that either $u = 0$ or $u' = 0$, and thus prevent the solver from producing unphysical divergent terms.

Before proceeding, we will show that solutions to this problem exist and are unique. Note that while construction of a numerical solution gives evidence for the existence of a solution to the continuum equations, uniqueness is not easy to verify numerically, and an analytical proof is highly desirable. While the uniqueness proof is general, the existence proof requires a more detailed analysis of the Hamiltonian constraint, and in the spinning case we will deal with only a single trumpet (we do however expect that the same procedure can be generalized to multiple spinning and boosted black holes).

We first prove uniqueness. Assume we have two positive solutions, ψ_1 and ψ_2. Subtract the equations to get

$$\tilde{\nabla}^2(\psi_1 - \psi_2) = -\frac{1}{8}\tilde{A}_{ij}\tilde{A}^{ij}(\psi_1^{-7} - \psi_2^{-7}).$$

We assume $\psi_{12} = \psi_1 - \psi_2$ goes to zero at both ends (they satisfy the same boundary conditions, and we saw in the preceding discussion that there are no other divergent terms in the solution). If ψ_{12} is not identically zero, it must have a positive maximum or a negative minimum.

Neither of these is compatible with the equation (leading to different signs on the left and right-hand side).

We now provide the outline of an existence proof. The maximum principle tells us that a solution, if it exists, cannot have an interior minimum. As $r \to \infty$ our boundary condition is that $\psi \to 1$, and so a solution, if it exists, satisfies $\psi \geq 1$. Therefore

$$\tilde{\nabla}^2 \bar{\psi} = -\frac{1}{8} K_{ij} K^{ij}$$

is a supersolution, i.e., it satisfies $\tilde{\nabla}^2(\bar{\psi} - \psi) \leq 0$ and $\bar{\bar{\psi}} = 1$ is a subsolution, i.e., $\tilde{\nabla}^2(\bar{\bar{\psi}} - \psi) \geq 0$, and, of course $\bar{\psi} > 0$. Finally, the solution with linear momentum $P = 0$ lies between. Therefore, as we change P the solution is trapped between the sub- and supersolution. The supersolution diverges as r^{-4} as $r \to 0$, proving that the true solution cannot have any divergence stronger than r^{-4}, and, in particular, that there are no logarithmic divergences. This allows us to posit an ansatz for ψ consistent with the allowed blowup powers, and then check by consistency with the full Hamiltonian constraint which of those survive to the full solution; and this leads to the $r^{-1/2}$ behavior determined in Sec. III. This completes our outline of an existence proof, which holds for single and multiple-black-hole solutions. The only complication arises when the trumpet has angular momentum, but we will deal with this case in Sec. V. A more rigorous proof along the lines of that for the wormhole-puncture case [35,37] remains to be constructed, and would be an interesting topic for future work.

Having proved that solutions to this system exist and are unique, we now must find them numerically. One potential problem that is apparent from Eq.. (19) is that the D_i source terms involve half-integer powers of r near the puncture, which affects the accuracy of the elliptic solver. Concretely, the D_0 term will lead to a $r^{3/2}$ contribution to the solution, which we expect to limit the solver to 1.5-order accuracy near the puncture, and the D_1 term will lead to a $r^{1/2}$ contribution, which we expect will limit the solver the 0.5-order accuracy near the puncture [46], and appears at a lower order than the $r^{\sqrt{2}-1/2} \approx r$ term that we have already accounted for in the ψ_{s2} ansatz.

These expectations are borne out in our results. Figure 3 shows the convergence behavior of the L_2 norm for the entire solution. We find that the convergence is at less than first-order, consistent with the half-order convergence predicted above. (Since we no longer have an analytic solution to compare with, we evaluate the convergence by comparisons between solutions with successive numbers of collocation points. We chose to sample N in multiples of four, and therefore display the L_2 norm of $(u_{N+4} - u_N)$ in the figure.) However, if we include in the L_2 norm only that part of the computational domain that is outside the apparent horizon of the black hole (located approximately at $r = 0.77$ m), then the errors show exponential convergence up to about $N = 32$. For higher numbers of collocation points the convergence rate deteriorates, and for the larger values of N shown in the figure the results are consistent with fourth-order convergence. This demonstrates that the behavior near the puncture limits the accuracy of the solution, but that this limitation is essentially localized within the black hole.

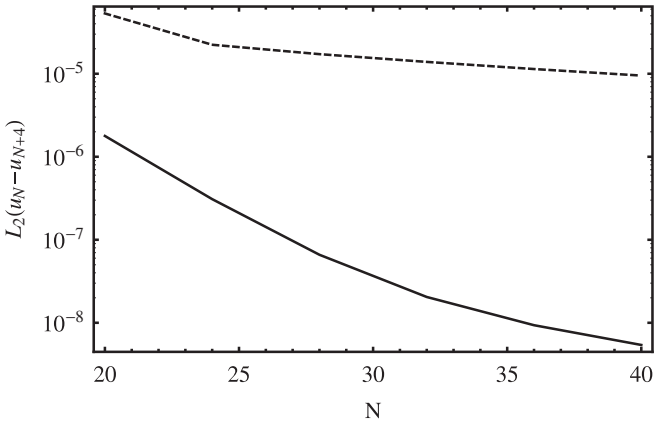

FIG. 3. The error behavior of the Hamiltonian-constraint solution for a single boosted trumpet. The dashed line shows the convergence of the L_2 norm over the entire domain, while the solid line shows the L_2 norm for the region of the domain outside the black-hole horizon. See text for more details.

The D_1 term is due to the A_5/r^5 term in $\tilde{A}_{ij}\tilde{A}^{ij}$ (which is in turn due to the cross-term between the Schwarzschild and Bowen-York extrinsic curvatures). If we remove these cross terms from the source function, we obtain the convergence behavior shown in Fig. 4; we now see, as expected, that for $N > 32$ the convergence approaches 1.5-order over the entire domain, consistent with the earlier discussion. Unfortunately, this solution does not represent

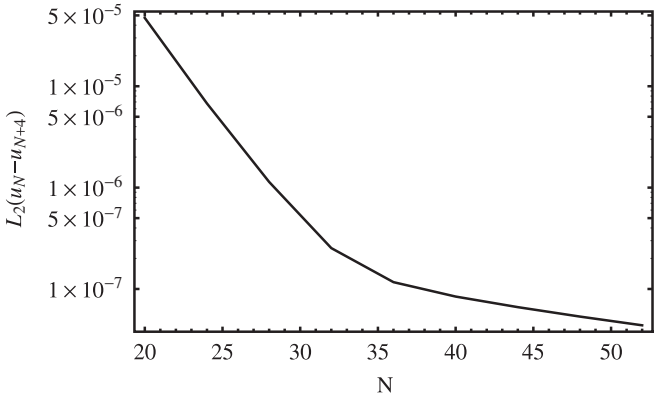

FIG. 4. The error behavior of the Hamiltonian-constraint solution for a single boosted trumpet, with the r^{-5} term removed from the source term. The solution displays clean exponential convergence up to about $N = 32$, and then the convergence deteriorates to 1.5-order (see text).

the correct conformal factor for a boosted Bowen-York trumpet puncture.

Although the inclusion of the Bowen-York extrinsic curvature limits the accuracy of our solver near the puncture, the solution is still very accurate over most of the computational domain, and is anyway accurate enough for most practical purposes everywhere. If one wished to produce yet more accurate solutions, one option would be to use a coordinate transformation from r to X that lead to the solution near the puncture being expanded in powers of $r^{1/2}$. However, for the purposes of this paper, such accuracy is not required, and we simply make this observation for future use.

V. SINGLE SPINNING BOWEN-YORK TRUMPETS

The construction of a solution for a single spinning Bowen-York puncture trumpet is complicated by the fact that the Bowen-York extrinsic curvature for a spinning black hole diverges as $1/r^3$ near the puncture. In this case, the behavior of the conformal factor near the puncture *will* be modified by the presence of the Bowen-York term. However, we will show that it is possible to determine the angular dependence of the divergent term in the conformal factor from a *local* one-dimensional ODE, which can be easily solved to construct the appropriate ansatz for a full numerical solution.

A. Angular dependence at the puncture

For convenience in what follows, we will express the problem in spherical coordinates. We will assume that the conformal factor now behaves as $\psi \sim D(\theta)/\sqrt{r}$ as $r \to 0$. The square of the conformal extrinsic curvature that appears in the Hamiltonian constraint is now

$$A^2 \equiv \tilde{A}^{ij}\tilde{A}_{ij} = \frac{6C^2}{r^6} + \frac{18S^2(1-\cos^2\theta)}{r^6}, \qquad (20)$$

where S is the angular momentum of the black hole. Note that in this case there are no cross terms.

To extend our earlier existence proof to the spinning case, we need to take into account the change in the divergent term in the conformal factor. We start by proving a monotonicity condition for the Hamiltonian constraint with these boundary conditions. More precisely, Let $A_1^2 = A^2(C, S_1)$ and $A_2^2 = A^2(C, S_2)$, where $S_2 > S_1$. Since $A_2^2 \geq A_1^2$, then $\psi_2 \geq \psi_1$. This means that, if we fix C and pump up S, the conformal factor monotonically increases.

The proof is as follows. Subtract the two solutions to get

$$\tilde{\nabla}^2(\psi_2 - \psi_1) + \frac{1}{8}[A_2^2\psi_2^{-7} - A_1^2\psi_1^{-7}] = 0.$$

Now multiply across by r^m where m lies between $1/2$ and 1, and find an equation for $\xi = r^m(\psi_2 - \psi_1)$. We find that

$$\tilde{\nabla}^2\xi - \frac{m}{r}\partial_r\xi - \frac{m-m^2}{r^2}\xi + \frac{r^m}{8}[A_2^2\psi_2^{-7} - A_1^2\psi_1^{-7}] = 0. \qquad (21)$$

We can see that ξ vanishes both at $r = 0$ and at infinity. The quantity ξ can never be negative because, if it were, it would have a negative minimum, and this cannot happen. Let us assume that it does have such a negative minimum. Let us see what happens to Eq. (21) at that point. We have $\nabla^2\xi \geq 0$, $-m/r\partial_r\xi = 0$, $-(m-m^2)/r^2\xi > 0$, and $+r^m/8[A_2^2\psi_2^{-7} - A_1^2\psi_1^{-7}] \geq 0$. The last term is the only slightly tricky term. If $\xi < 0$, then $\psi_2 < \psi_1$ and $\psi_2^{-7} > \psi_1^{-7}$. Since we assume $A_2^2 \geq A_1^2$, this term is also nonnegative and the sum cannot add up to zero.

Now we want to consider how $D(\theta)$ behaves, where we assume $\psi = D(\theta)/\sqrt{r} + O(\sqrt{r})$ near the origin. When we substitute into the Hamiltonian constraint, we get the following equation for $D(\theta)$:

$$D'' + \frac{D'}{\tan(\theta)} - \frac{1}{4}D + \frac{1}{8D^7}[6C^2 + 18S^2(1-\cos^2\theta)] = 0, \qquad (22)$$

where D'' is second derivative with respect to θ. This is defined on the interval $0 \leq \theta \leq \pi$, but will be symmetric around $\pi/2$. At a maximum we have

$$D^8 < 1/2[6C^2 + 18S^2(1-\cos^2\theta)],$$

while at a minimum we have

$$D^8 > 1/2[6C^2 + 18S^2(1-\cos^2\theta)].$$

Therefore the maximum should occur at $\pi/2$ and the minimum at $\theta = 0$ and D satisfies

$$3C^2 \leq D^8 \leq [3C^2 + 9S^2].$$

These upper and lower bounds allow our earlier existence proof to go through unchanged.

Equation (22) should be read as a one-dimensional second-order equation for $D(\theta)$ on the interval $0 \leq \theta \leq \pi/2$, with Neumann boundary conditions, i.e., $D' = 0$ at both ends.

A solution of Eq. (22) provides the necessary information to construct a single spinning Bowen-York puncture trumpet. The most important feature of Eq. (22) is that it is *local*: we need only solve a simple one-dimensional ODE in order to calculate the requisite boundary information—*regardless of the linear momentum of the black hole, and regardless of the presence or otherwise of other black holes in the data*.

B. Solution of the nonlinear angular-dependence ODE

We solve the nonlinear ODE Eq. (22) by linearizing and solving iteratively. The average of the upper and lower bounds is used as an initial guess. A simple application of the `NDSolve` function in Mathematica suffices to produce an accurate solution. The solution for $S/M^2 = 1$ is

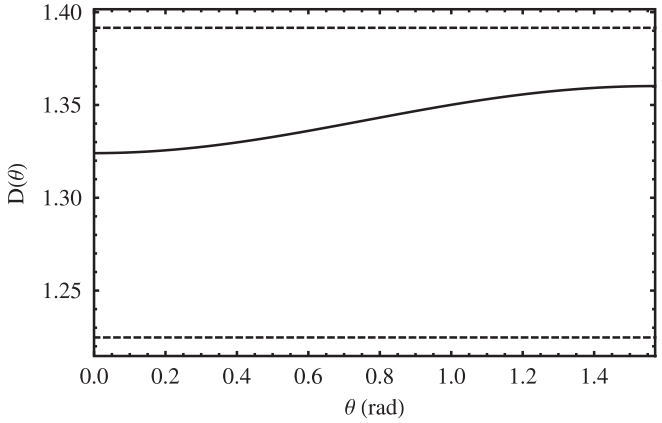

FIG. 5. The solution $D(\theta)$ for $C^2 = 27/16$ and $S = 1.0$. The upper and lower bounds, $D^8_{\rm lower} = 3C^2$ and $D^8_{\rm upper} = 3C^2 + 8S^2$ are shown with dashed lines.

shown in Fig. 5; the function $D(\theta)$ is seen to lie well within the upper and lower bounds derived in the previous section.

Figure 6 shows the maximum value of $D(\theta)$, which occurs at $\theta = \pi/2$, as a function of the angular momentum S. The figure shows the upper bound on the solution, $(3C^2 + 9S^2)^{1/8}$, for comparison. The maximum behaves as expected, i.e., grows as $S^{1/4}$ for large S. When S is small, the $3C^2$ term dominates, and the value approaches the Schwarzschild value of $\sqrt{3/2}$.

Now that we have calculated $D(\theta)$, we are able to solve the Hamiltonian constraint for both boosted and spinning Bowen-York trumpets. The conformal-factor ansatz is now provided by replacing the $\sqrt{3M/2r}$ term in (13) with $D(\theta)/\sqrt{r}$. In the numerical procedure to solve the Hamiltonian constraint, the derivatives of $D(\theta)$ required in the construction of $\tilde{\nabla}^2\psi_s$ are trivial to calculate in our `Mathematica`-based solver, because $D(\theta)$ is available from the solution to (22) as an `InterpolatingFunction` to whatever precision is required.

Note, however, that for the spinning case we do not know the next-to-leading order behavior of the solution to the Hamiltonian constraint (the coefficient of the $r^{\sqrt{2}-1/2}$ term) as we did in the boosted case, and this will restrict the accuracy of our solver to that given by the ψ_{s1} ansatz in Sec. IV, and of course the magnitude of this term will grow with the value of the angular momentum. For this reason, high accuracy is difficult to achieve for extremely high values of the spin. For the data sets studied in this paper we consider angular momenta no higher than $S = 10M^2$, which corresponds to $S/M^2 \approx 0.924$. We will now discuss the junk radiation content of our data sets in more detail.

VI. RADIATION CONTENT OF TRUMPET-PUNCTURE DATA

Bowen-York black holes can be considered as Kerr or boosted Schwarzschild black holes, plus some unphysical radiation content, which either falls into the black hole or radiates away as junk radiation. We can estimate the radiation content of the data as [47,48]

$$E_{\rm rad} = \sqrt{E^2_{\rm ADM} - P^2} - M. \tag{23}$$

To evaluate this quantity we first need an estimate of the black hole's mass M. The standard way to calculate this is via the area of the apparent horizon of the black hole. We calculate the irreducible mass, $M_{\rm irr} = \sqrt{A/16\pi}$ and then use the Christodoulou formula [49] to estimate the total mass of a black hole with angular momentum S,

$$M^2 = M^2_{\rm irr} + \frac{S^2}{4M^2_{\rm irr}}. \tag{24}$$

For boosted wormhole data, the black-hole mass can also be estimated by calculating the ADM mass at the

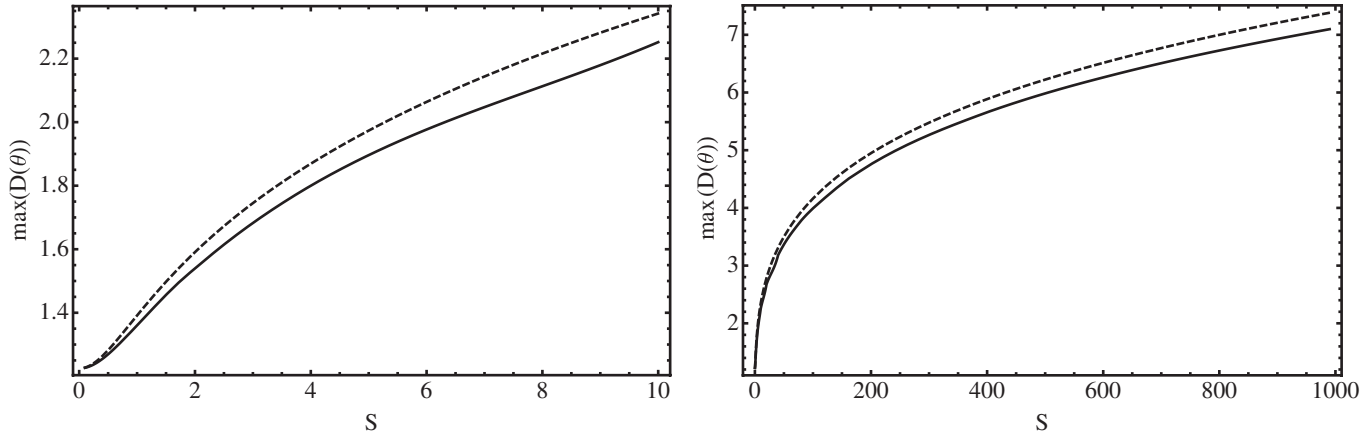

FIG. 6. Values of the maximum value of $D(\theta)$ (at $\theta = \pi/2$) as a function of the angular momentum S, shown with a solid line. Also shown as a dashed line is the upper bound. The maximum behaves as $S^{1/4}$ for large S.

extra asymptotically flat end; one can see by performing an inversion transformation on the Bowen-York extrinsic curvature that its contribution at the extra end falls off as r^{-4}, and therefore we expect that it contributes very little junk radiation in the second copy of the exterior space. This suggests that the ADM mass evaluated at the second asymptotically flat end (i.e., at the puncture) will provide a good measure of the mass, and this has been confirmed by numerical observations [33], and the ''ADM puncture mass'' has become a standard tool in wormhole-puncture data [14,34,40,41].

There are two drawbacks of the ADM puncture mass. One is that it does not provide a good estimate of the mass for spinning black holes, since in that case the Bowen-York extrinsic curvature has the same falloff behavior at both asymptotically flat ends, $O(r^{-3})$, and contributes roughly the same junk radiation into both exterior regions. We have verified this in numerical tests, where we find that the ADM puncture mass for spinning-Bowen-York-puncture data sets equals the ADM mass calculated at spatial infinity to within the numerical accuracy of the solver ($\approx 10^{-8}$).

The other disadvantage of the ADM puncture mass, which applies in general to wormhole-puncture data, is that the mass cannot be prescribed *a priori*, because the relationship between the mass parameter m and the black-hole mass M is nonlinear. In order to construct Bowen-York wormhole punctures with specific masses, an iteration procedure must be used.

The situation appears to be quite different in the trumpet case. Here the mass parameter m *does* seem to prescribe the mass of the black hole, at least for boosted black holes. This is presumably related to the fact that the Bowen-York extrinsic curvature does not affect the geometry of the trumpet, irrespective of the value of the linear momentum. This interesting (and useful) property of the boosted Bowen-York trumpet deserves further study.

The same cannot be the case for spinning black holes, however, where the coefficient of the singular term in the conformal factor is an angular function of the spin. We could propose a mass based on the area of the trumpet, but this is not necessarily useful, because we do not know the relationship between the trumpet area and the black-hole mass for spinning black holes. For spinning black holes we must make use of the mass calculated from the area of the apparent horizon, Eq. (24).

We are now in a position to estimate the junk-radiation content of our boosted and spinning trumpet data sets.

Figure 7 shows the estimate of the radiation content for boosted wormhole and trumpet initial-data sets. We see that the results are almost identical for both classes of initial data. This also provides further evidence of the equivalence of the mass estimates that were used for each class of data. These results can further be compared with those for other families of boosted Bowen-York data [40,47,48], for which the values of the junk-radiation content appear to be very similar.

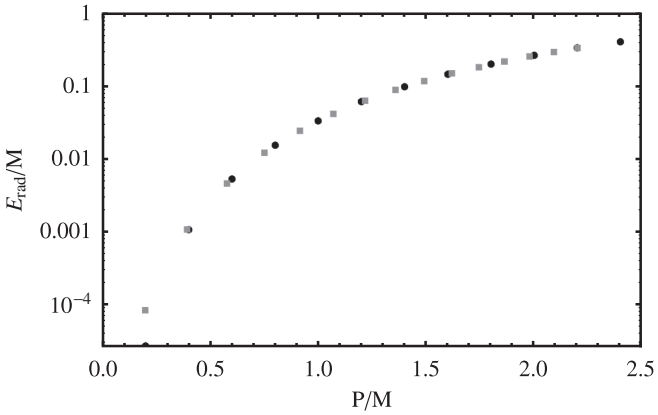

FIG. 7. Estimate of the radiation energy content of boosted black-hole initial data sets. The grey squares indicate wormhole data, and the black circles indicate trumpet data. The results for both Bowen-York trumpets and wormholes are shown. The results are identical at the level of accuracy of the data: as one might expect, the use of a trumpet versus a wormhole topology does not affect the radiation content of the data.

Figure 8 shows the same quantity estimated for spinning trumpet data sets. If we compare with the results in [47,48] we see that the use of the trumpet topology does not noticeably change the junk-radiation content.

It was pointed out in [26,50] that taking the limit as $m \to 0$ while keeping S fixed is equivalent to keeping m fixed and taking the limit $S \to \infty$. In other words, by simply removing the Schwarzschild trumpet term from the extrinsic curvature, we can construct data equivalent to the $S \to \infty$ limit. Furthermore, since we know that the horizon is located at the puncture for these data, we can directly calculate the apparent-horizon area to high accuracy from our angular function $D(\theta)$:

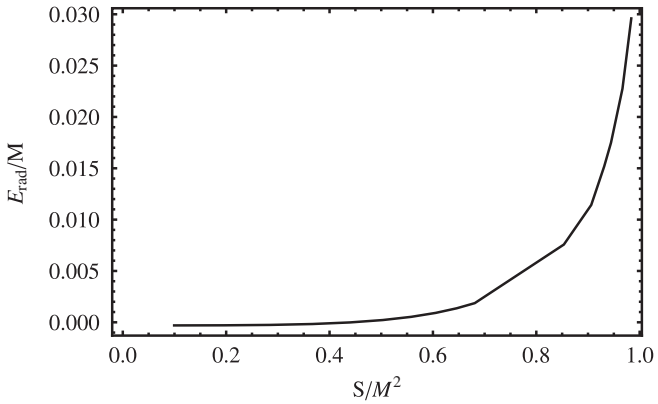

FIG. 8. Estimate of the radiation energy content of spinning black-hole-trumpet initial data sets, including the extreme limit, at which $S/M^2 = 0.9837$ and $E_{\rm rad} = 0.0296$, i.e., the junk radiation never consists of more than 2.96% of the energy of the spacetime.

$$A = \lim_{r\to 0} \int \psi^4 r^2 \sin(\theta) d\theta d\phi \tag{25}$$

$$= 2\pi \int D^4(\theta) \sin(\theta) d\theta. \tag{26}$$

We do this and find that $S/M^2 = 0.9837$, in precise agreement with the results in [27], although we note that via Eq. (22) one can calculate this value to arbitrary accuracy. We also find that $S/M_{\rm ADM}^2 = 0.928$, again in agreement with the results in [27]. These numbers provide upper and lower bounds on the spin of the final Kerr black hole, after the junk radiation has left the spacetime. We evolved these data, and found that less than 0.05% of the energy in the initial slice was radiated away, and therefore the rest of the junk radiation falls into the black hole (in agreement with the observations in [26]), and the final Kerr black hole has a spin parameter of $0.928 \leq a/m \leq 0.929$. Note also that it follows from the results in [26,50] that the high-angular-momentum limits of the wormhole and trumpet Bowen-York data are equivalent.

VII. BINARY TRUMPETS

We now wish to construct data for two Bowen-York trumpets. The linearity of the momentum constraint with $K = 0$ allows us to superimpose any number of solutions: for each black hole we simply include both the Schwarzschild trumpet extrinsic curvature and the Bowen-York extrinsic curvature to obtain a valid solution of the momentum constraint. For black holes located at $\mathbf{r}_1$ and $\mathbf{r}_2$, the extrinsic curvature is therefore

$$\tilde{A}_{ij} = \tilde{A}^S_{ij}(\mathbf{r} - \mathbf{r}_1) + \tilde{A}^{\rm BY}_{ij}(\mathbf{r} - \mathbf{r}_1; \mathrm{P}_1) + \tilde{A}^S_{ij}(\mathbf{r} - \mathbf{r}_2) + \tilde{A}^{\rm BY}_{ij}(\mathbf{r} - \mathbf{r}_2; \mathrm{P}_2). \tag{27}$$

We once again need a suitable ansatz for the conformal factor. The first obvious choice is to generalize the ansatz used for a single black hole and try

$$\psi_s^{\rm guess} = w_1(r_1)\left[\sqrt{\frac{R_{01}}{r_1}} + R_{01}^{3/2}\left(m_1 + \frac{R_{01}}{\sqrt{2}}\right)^p r_1^q\right] \times w_1(r_2)\left[\sqrt{\frac{R_{02}}{r_2}} + R_{02}^{3/2}\left(m_2 + \frac{R_{02}}{\sqrt{2}}\right)^p r_2^q\right] + w_2(r_1)w_2(r_2), \tag{28}$$

where $R_{0i} = 3m_i/2$, $p = -1 - \sqrt{2}$ and $q = \sqrt{2} - 1/2$, and where the w_2 weightings are multiplied so that the resulting function is zero at each puncture, and asymptotes to unity far from the source.

We saw in Sec. IV that the requirement that $u = 0$ at the puncture removed any logarithmically divergent terms from the solution, but this was possible only because the problematic part of the source term was linear in u: setting $u = 0$ removed that term. In the binary case, with the ansatz we have chosen, this is not necessarily so simple. Near one puncture (let us choose r_1) the conformal factor behaves as $\psi = \sqrt{3m/2r} + F + u$, where F is the contribution from the second term in Eq. (28). This could also generate a logarithmic term. One solution would be to determine the appropriate value of u at the puncture such that this term no longer contributes (i.e., $u(r_1 = 0) = -F$), and enforce this in the solver, or hope that the solver finds that value.[1] An alternative solution is to choose an additional weighting factor so that in fact $A = 0$, and to again impose our standard $u = 0$ or $u' = 0$ boundary condition at the puncture; this is the approach that we will follow.

To solve the Hamiltonian constraint numerically for binary trumpets, we adopt similar coordinates in our pseudospectral solver as developed in [23] for use with wormhole-puncture data. For an equal-mass binary with punctures located on the x-axis at $x = \pm b$, we make the coordinate transformation

$$x = \frac{2b(5 + X(2 + X))Y}{(1 + Y^2)(3 + X)(X - 1)}, \tag{29}$$

$$y = \frac{4b(1 + X)(Y^2 - 1)\cos\phi}{(1 + Y^2)(X^2 + 2X - 3)}, \tag{30}$$

$$z = \frac{4b(1 + X)(Y^2 - 1)\sin\phi}{(1 + Y^2)(X^2 + 2X - 3)}. \tag{31}$$

In these coordinates $X = 1$ corresponds to spatial infinity. The points $(X, Y) = (-1, \pm 1)$ correspond to the puncture locations at $x = \pm b$. The line along the x-axis between the two punctures is mapped to the plane $X = -1$. For a full description of this coordinate system and its properties, the reader is referred to [23].

These coordinates make it particularly simple to apply additional weighting factors that remove at each puncture the contribution to the conformal-factor ansatz from the other puncture. The weights we choose are $w_1 \to w_1 \cos[(\pi/4)(1 \pm Y)]^4$.

As an example, we construct data for the same configuration as in the "D10" case studied in [52]: the punctures are located at $x = \pm 5M$, and the momenta are $\mathbf{P} = (\mp 9.80376 \times 10^{-4}, \pm 0.0961073, 0)$. The specific momenta are not important for this test; we simply choose the same numbers to allow a direct comparison of the initial data sets.

The solution u for this system is shown in Fig. 9, represented in the coordinates (29)–(31), along the plane $z = 0$ ($\phi = 0$).

The convergence of the solver for these data is shown in Fig. 10. The results indicate surprisingly good convergence

[1] Research performed concurrently with that in this paper found that indeed the solver does appear to locate this value [51]

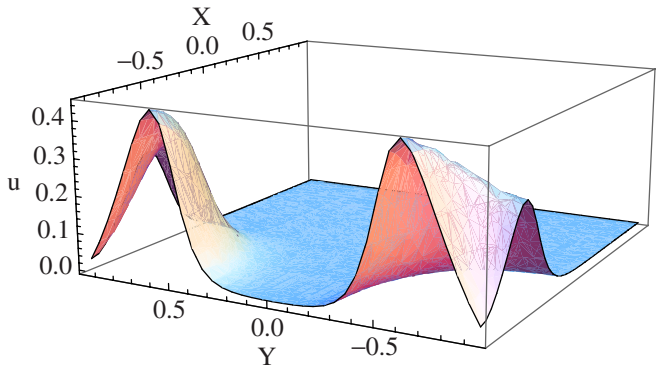

FIG. 9 (color online). The function u for the binary configuration described in the text, represented in the bipolar coordinates used in the pseudospectral solver. Note that $X = 1$ corresponds to spatial infinity, while $X = -1$, $Y = \pm 1$ are the puncture locations.

in comparison to the single-black-hole cases. This may be due to a cancellation in some other problematic terms in the binary case. For example, far from the binary the Hamiltonian-constraint source term will closely resemble that of a single spinning black hole; similar cancellation affects may play a role throughout the computational domain.

We can calculate the ADM mass of the system by noting that near spatial infinity, $\psi \sim 1 + M_{\rm ADM}/(2r)$, and obtain the ADM mass from the radial derivative of u as $r \to \infty$. As an indication of the accuracy of our solver, and of the level of difference between wormhole and puncture binary data, the ADM masses for the wormhole and puncture data with the same choice of black-hole mass, separation and linear momenta, were 0.9897136 and 0.989706, respectively. If we calculate the binding energies ($E_b = M_{\rm ADM} - M_1 - M_2$) for these two data sets, they are $E_{b,\rm wormhole} = -0.0102864$ and $E_{b,\rm trumpet} = -0.0102939$. This demonstrates that these data sets are physically extremely close—with the added advantage in the trumpet case that the black-hole masses could be specified directly through the mass parameter, while in the wormhole case they had to be calculated by a nonlinear iteration procedure [34,52].

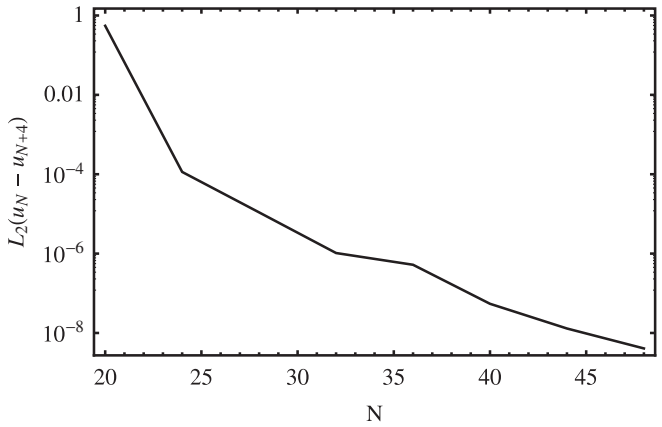

FIG. 10. Error behavior for a binary configuration. The plot shows the L_2 norm of the difference between solutions produced with N and $N + 4$ collocation points. Only values along the $z = 0$ plane are included in the calculation, but since the punctures lie in this plane, this plot shows the dominant error behavior for the solution.

VIII. NUMERICAL EVOLUTION OF THE DATA

Having proposed and produced a new class of black-hole initial data, and claimed certain gauge and physical properties for them, we now need to evolve a set of trumpet binary data and put our claims to the test. In particular, there are two questions we wish to answer:

(1) We expect that the trumpet data are in coordinates closer to those preferred by the moving-puncture method than wormhole data; is this true?
(2) Do the wormhole and trumpet data describe the same *physical* situation, or, in practical terms, do they produce the same gravitational-wave signal?

We evolve the data using the same version of the BAM code [34,53] used to produce the results in [52], with which we compare the gravitational waveform. In the notation of those works. we use the same $N = 64$ grid layout as used for the D10 simulation; see Table 1 in [52].

A. Gauge changes

The first question that we have posed above is difficult to answer. The data that we have produced are maximally sliced, while in the moving-puncture method one usually deals with 1 + log slicing, and the data will quickly cease to be maximally sliced and will asymptote to their appropriate 1 + log form. In addition, the punctures are initially stationary, but will pick up speed once the evolution begins; this constitutes yet another change of gauge. These gauge changes may be "larger" than those induced by the transition of wormhole data to trumpet form—whatever larger means in the context of gauge changes.

However, we can perform one simple test to quantify the change in gauge between the two sets of data. In wormhole data, the apparent horizons of the two black holes are located on surfaces with coordinate radii close to $r \approx m/2$, where m is the mass parameter in the wormhole-puncture conformal ansatz (5). For trumpet data, on the other hand, the horizon is at about $r \approx 0.78M$. If we evolve both wormhole and trumpet data with a variant of 1 + log slicing that will asymptote to maximal slicing for a stationary spacetime, then we expect that the horizon radius will stay roughly fixed in the trumpet case, while in the wormhole case it will increase quickly to a value close to $r \approx 0.78M$. (The rapid expansion of the horizon early in simulations is standard in moving-puncture simulations; see, for example, [2,3,34].)

The slicing condition that approaches maximal slicing for a stationary solution is

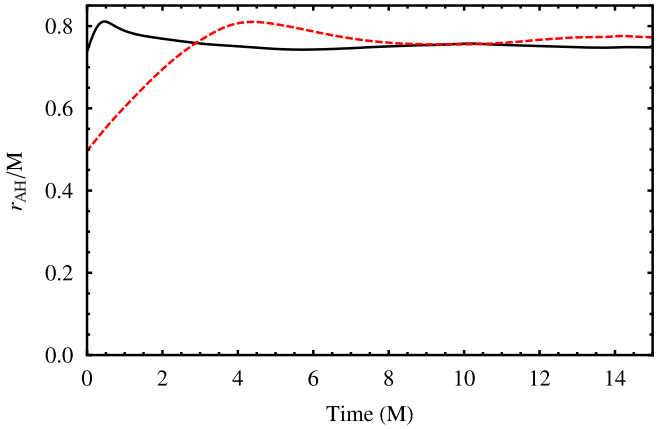

FIG. 11 (color online). Coordinate radius of the apparent horizon as a function of time, for one of the black holes in a binary evolution. The data are initially maximally sliced. At early times the slicing will deviate from $K = 0$, but in a stationary situation would return to maximal slicing within $t \approx 10M$. As expected, the apparent-horizon radius shows much less deviation for trumpet data (solid line) than for wormhole data (dashed line).

$$\partial_t \alpha = -2\alpha K, \tag{32}$$

i.e., the standard 1 + log slicing used in moving-puncture simulations, but *without* the shift term on the left-hand side. With this gauge condition the data will deviate from maximal slicing at early times, but will again be approximately maximally sliced after about $t = 10M$ of evolution [19]. In addition we set $\eta = 0$ in the $\tilde{\Gamma}$-driver shift condition, to minimize additional gauge-related growth in the horizon [19,34]. The results are shown in Fig. 11, and are as expected: in the wormhole case the horizon radius grows to about $0.75M$ within $10M$ of evolution, while in the trumpet case the horizon radius remains close to that value at all times. The additional oscillations may be due to other gauge effects, but are of much smaller magnitude than the main effect we have just described.

B. Junk radiation

We construct two sets of binary initial data (wormhole and trumpet) for a binary with initial coordinate separation of $D = 10M$. We adjust the initial momenta such that both sets of data exhibit quasicircular inspiral. (We find that different values of the initial momenta are required for each class of data; the reasons for these small differences are at least partially due to the coordinate change made manifest by the different apparent horizon sizes mentioned previously, and deserve further investigation in future work.) We then evolve using standard moving-puncture gauge choices, i.e., the full 1 + log slicing condition, $(\partial_t - \beta^i \partial_i)\alpha = -2\alpha K$, and with $\eta/M = 2$ in the $\tilde{\Gamma}$-driver condition. We now wish to evaluate the differences in the gravitational-wave signal between simulations using each data set.

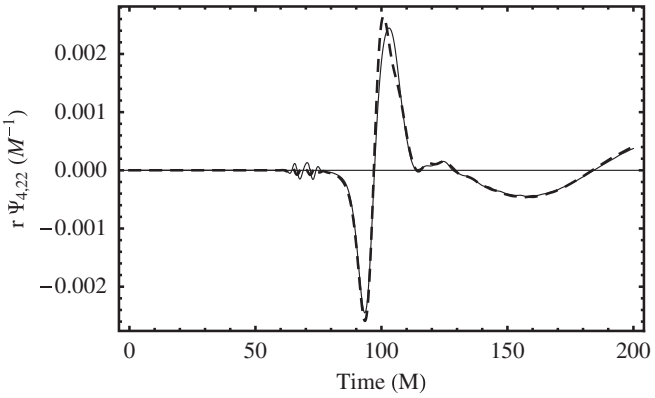

FIG. 12. Junk-radiation pulse from binary wormhole and trumpet data, with initial separation of $D = 10M$, and radiation-extraction radius of $R_{ex} = 90M$. The trumpet-data results are shown with the thick dashed line, and the wormhole-data results are shown with the grey continuous line. As suggested by Fig. 7, the junk-radiation content of both data sets is of comparable magnitude.

The first point of comparison is the burst of junk radiation at the beginning of the simulation. Based on the results in Sec. IV, we would expect that the junk radiation is the same in wormhole and trumpet data. Figure 12 shows the pulse of junk radiation in the spin-weight -2, ($\ell = 2$, $m = 2$) mode of $r\Psi_4$, as calculated $R_{ex} = 90M$ from the source. (Full details of the wave-extraction procedure used in the code are given in [34].) Although the junk pulses from the two data sets are not identical, they are very similar; it is certainly not possible to definitively claim that one type of data contains less junk radiation than the other.

We emphasize that this result is not merely a demonstration of a result that we know to be true. The estimate of the radiation content of the initial-data sets, based on the initial data alone, is no more than that: an estimate. It is only by evolving the data in a full general-relativistic simulation that we can be certain that this (or any other) property that we claim for a new initial-data set actually holds.

C. Inspiral-merger-ringdown signal

We now consider the full inspiral-merger-ringdown GW signal generated by the inspiral and coalescence of the two black holes. In this simulation the binary completes about five orbits before merger.

We focus of the dominant ($\ell = 2$, $m = 2$) spin-weighted spherical harmonic mode of $r\Psi_4$, as extracted at $R_{ex} = 90M$ from the source. Figure 13 shows separately the inspiral and merger-ringdown portions of the real part of $r\Psi_{4,22}$. (The plot begins after the junk radiation has passed through the $R_{ex} = 90M$ radiation-extraction sphere.) The time has been shifted so that the maximum amplitude occurs at $t = 0$.

The figure includes both the wormhole- and trumpet-data results. The results are indistinguishable, except for a

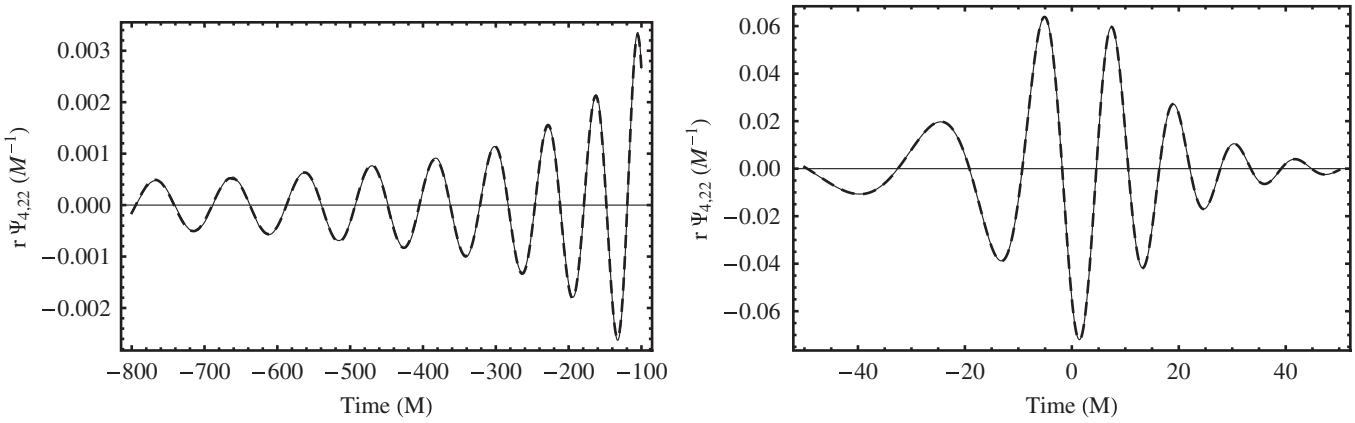

FIG. 13. Comparison of the inspiral and merger waveforms. The trumpet-data results are shown with the thick dashed line, and the wormhole-data results are shown with the grey continuous line. A time and phase shift have been applied so that the amplitude maxima occur at the same time, at which time the waveforms are in phase.

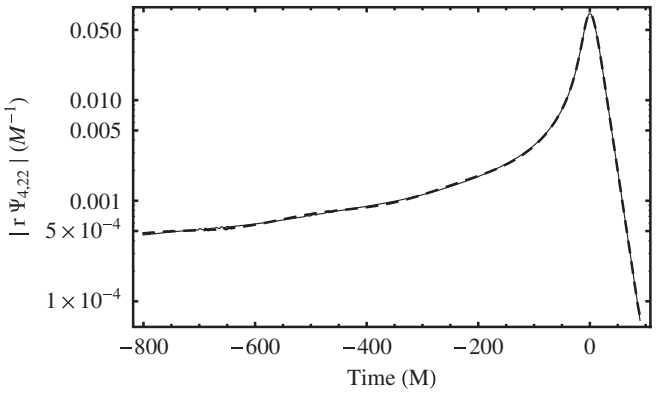

FIG. 14. The amplitude of $r\Psi_{4,22}$, as calculated from moving-puncture simulations of wormhole and trumpet-puncture initial data, with initial separation of $D = 10M$. The waveforms are shifted such that the maxima in the amplitude occur at the same time. The thick dashed line shows the trumpet-data results, while the continuous grey line shows the wormhole-data results.

very small amount of dephasing early in the signal, due to the slightly different effective choice of initial parameters.

Figure 14 shows the amplitude of $r\Psi_{4,22}$ for the wormhole and trumpet data. In this case the lines can be distinguished due to the slightly different eccentricities present in the two data sets. Once again it is clear, however, that the two waveforms agree extremely well; they certainly agree well within the error levels discussed in the recent Samurai project [4], which demonstrated that waveforms that agree to this level are well within the accuracy requirements for detection and parameter estimation with first- and second-generation ground-based GW detectors.

IX. DISCUSSION

In this work we have extended the puncture method to produce *trumpet* data for boosted, spinning and binary black holes based on the Bowen-York extrinsic curvature. In the boosted case the generalization is straightforward, and in the spinning case a simple one-dimensional nonlinear ordinary differential equation must be solved to determine the angular dependence of the asymptotic trumpet geometry.

We have discovered one surprising advantage of trumpet data over their wormhole counterpart, which is that the mass of a boosted Bowen-York trumpet can be prescribed analytically by the mass parameter in the conformal-factor ansatz used to solve the Hamiltonian constraint. This is a great computational advantage over the wormhole case, where the mass parameter must be iterated to produce data that contain black holes with specific desired masses. This relationship could not however be extended to spinning black holes.

The motivation to produce black-hole initial data in trumpet form is that this is the topology that is preferred by the gauge conditions that are used in the moving-puncture method, which is itself the most popular method for simulating black-hole binaries. Although we do not expect (and did not find) any dramatic differences in the properties of black-hole simulations between wormhole and trumpet data, the construction of these data are an important first step towards ideal initial data for puncture simulations. Such ideal data will be in the 1 + log gauge (or whatever slicing condition is ultimately used to evolve the data, one natural alternative being hyperboloidal slicing conditions [44,54]), will represent true boosted Schwarzschild or Kerr black holes, and will be in trumpet form. In this work we have made the simplest step in this direction, i.e., we have produced trumpet data, but they are maximally sliced and represent only approximations to boosted Schwarzschild and Kerr black holes.

Efforts in these other directions have already been made. Data for superposed Kerr punctures have, for example, been presented in [31], and superposed boosted Schwarzschild punctures have been used in [55]; non-

conformally-flat data that attempt to include the GW signal from the earlier inspiral of the binary have been proposed in [56]. Work has also been done in producing non-conformally-flat data with excision techniques [27,57]. It is also now known how to produce 1 + log trumpet-puncture data for a single Schwarzschild black hole [19]. It is likely that a combination of all of these approaches will be necessary to produce the optimal data for puncture simulations.

ACKNOWLEDGMENTS

We thank Sergio Dain for discussions related to the extreme spinning-Bowen-York limit, and Frank Ohme and Julia Gundermann for a careful reading of the manuscript. M. H. and N. Ó. M. were supported by SFI grant 07/RFP/PHYF148. S. H. was supported in part as by VESF and the European Gravitational Observatory (EGO), by DAAD grant D/07/13385 and grant FPA-2007-60220 from the Spanish Ministerio de Educación y Ciencia. We thank LRZ (Munich), ICHEC (Dublin) and CESGA (Santiago de Compostela) for providing computational resources. M. H. thanks the University of the Balearic Islands for hospitality while some of this work was carried out.

[1] F. Pretorius, Phys. Rev. Lett. **95**, 121101 (2005).
[2] M. Campanelli, C. O. Lousto, P. Marronetti, and Y. Zlochower, Phys. Rev. Lett. **96**, 111101 (2006).
[3] J. G. Baker, J. Centrella, D.-I. Choi, M. Koppitz, and J. van Meter, Phys. Rev. Lett. **96**, 111102 (2006).
[4] M. Hannam *et al.*, Phys. Rev. D **79**, 084025 (2009).
[5] B. Aylott *et al.*, Classical Quantum Gravity **26**, 165008 (2009).
[6] M. Hannam, Classical Quantum Gravity **26**, 114001 (2009).
[7] T. W. Baumgarte and S. L. Shapiro, Phys. Rev. D **59**, 024007 (1998).
[8] M. Shibata and T. Nakamura, Phys. Rev. D **52**, 5428 (1995).
[9] R. Arnowitt, S. Deser, and C. W. Misner, in *Gravitation An Introduction to Current Research*, edited by L. Witten (John Wiley, New York, 1962), pp. 227–265.
[10] J. W. York, Jr., in *Sources of Gravitational Radiation*, edited by L. Smarr (Cambridge University Press, Cambridge, 1979), pp. 83–126.
[11] C. Bona, J. Masso, E. Seidel, and J. Stela, Phys. Rev. Lett. **75**, 600 (1995).
[12] M. Alcubierre, B. Bruegmann, D. Pollney, E. Seidel, and R. Takahashi, Phys. Rev. D **64**, 061501 (2001).
[13] M. Alcubierre *et al.*, Phys. Rev. D **67**, 084023 (2003).
[14] S. Brandt and B. Bruegmann, Phys. Rev. Lett. **78**, 3606 (1997).
[15] M. Hannam, S. Husa, D. Pollney, B. Bruegmann, and N. O'Murchadha, Phys. Rev. Lett. **99**, 241102 (2007).
[16] M. Hannam *et al.*, J. Phys. Conf. Ser. **66**, 012047 (2007).
[17] F. Estabrook *et al.*, Phys. Rev. D **7**, 2814 (1973).
[18] T. W. Baumgarte and S. G. Naculich, Phys. Rev. D **75**, 067502 (2007).
[19] M. Hannam, S. Husa, F. Ohme, B. Bruegmann, and N. O'Murchadha, Phys. Rev. D **78**, 064020 (2008).
[20] D. R. Brill and R. W. Lindquist, Phys. Rev. **131**, 471 (1963).
[21] J. M. Bowen, J. York, and W. James, Phys. Rev. D **21**, 2047 (1980).
[22] J. D. Brown and L. L. Lowe, J. Comput. Phys. **209**, 582 (2005).
[23] M. Ansorg, B. Bruegmann, and W. Tichy, Phys. Rev. D **70**, 064011 (2004).
[24] M. Boyle *et al.*, Phys. Rev. D **76**, 124038 (2007).
[25] S. Dain, C. O. Lousto, and R. Takahashi, Phys. Rev. D **65**, 104038 (2002).
[26] S. Dain, C. O. Lousto, and Y. Zlochower, Phys. Rev. D **78**, 024039 (2008).
[27] G. Lovelace, R. Owen, H. P. Pfeiffer, and T. Chu, Phys. Rev. D **78**, 084017 (2008).
[28] M. Volonteri *et al.*, Astrophys. J. **620**, 69 (2005).
[29] C. F. Gammie *et al.*, Astrophys. J. **602**, 312 (2004).
[30] S. L. Shapiro, Astrophys. J. **620**, 59 (2005).
[31] M. Hannam, S. Husa, B. Bruegmann, J. A. Gonzalez, and U. Sperhake, Classical Quantum Gravity **24**, S15 (2007).
[32] J. Thornburg, Classical Quantum Gravity **21**, 743 (2004).
[33] W. Tichy and B. Bruegmann, Phys. Rev. D **69**, 024006 (2004).
[34] B. Bruegmann *et al.*, Phys. Rev. D **77**, 024027 (2008).
[35] R. Beig and N. O. Murchadha, Classical Quantum Gravity **11**, 419 (1994).
[36] R. Beig and S. Husa, Phys. Rev. D **50**, R7116 (1994).
[37] S. Dain and H. Friedrich, Commun. Math. Phys. **222**, 569 (2001).
[38] T. W. Baumgarte, Phys. Rev. D **62**, 024018 (2000).
[39] M. Hannam, C. R. Evans, G. B. Cook, and T. W. Baumgarte, Phys. Rev. D **68**, 064003 (2003).
[40] M. Hannam and G. B. Cook, Phys. Rev. D **71**, 084023 (2005).
[41] M. Hannam, Phys. Rev. D **72**, 044025 (2005).
[42] J. D. Brown, Phys. Rev. D **77**, 044018 (2008).
[43] D. Garfinkle, C. Gundlach, and D. Hilditch, Classical Quantum Gravity **25**, 075007 (2008).
[44] F. Ohme, M. Hannam, S. Husa, and N. O. Murchadha, Classical Quantum Gravity **26**, 175014 (2009).
[45] B. Bruegmann, Gen. Relativ. Gravit. **41**, 2131 (2009).

[46] J. P. Boyd, *Chebyshev and Fourier Spectral Methods* (Dover Publications, New York, 2001), 2nd ed. (Revised), ISBN .
[47] G. B. Cook, Ph.D. thesis, University of North Carolina at Chapel Hill, Chapel Hill, North Carolina, 1990.
[48] G. B. Cook, J. York, and W. James, Phys. Rev. D **41**, 1077 (1990).
[49] D. Christodoulou, Phys. Rev. Lett. **25**, 1596 (1970).
[50] S. Dain and M. E. Gabach Clement, Classical Quantum Gravity **26**, 035020 (2009).
[51] J. D. Immerman and T. W. Baumgarte, arXiv:0908.0337.
[52] M. Hannam, S. Husa, U. Sperhake, B. Bruegmann, and J. A. Gonzalez, Phys. Rev. D **77**, 044020 (2008).
[53] S. Husa, J. A. Gonzalez, M. Hannam, B. Bruegmann, and U. Sperhake, Classical Quantum Gravity **25**, 105006 (2008).
[54] L. T. Buchman, H. P. Pfeiffer, and J. M. Bardeen, Phys. Rev. D **78**, 101501 (2008).
[55] M. Shibata, H. Okawa, and T. Yamamoto, Phys. Rev. D **78**, 101501 (2008).
[56] B. J. Kelly, W. Tichy, M. Campanelli, and B. F. Whiting, Phys. Rev. D **76**, 024008 (2007).
[57] G. Lovelace, Classical Quantum Gravity **26**, 114002 (2009).